FRONTIERS OF PHYSICS

RESEARCH ARTICLE
Volume 19 / Issue 4 / 43201 / 2024

Spin transport of half-metal Mn_2X_3 with high Curie temperature: An ideal giant magnetoresistance device from electrical and thermal drives

Bin Liu[1,*], Xiaolin Zhang[1,2,*], Jingxian Xiong[3], Xiuyang Pang[3], Sheng Liu[1], Zixin Yang[3],
Qiang Yu[3,5], Honggen Li[6], Sicong Zhu[1,4,†], Jian Wu[3,‡]

1 Hubei Province Key Laboratory of Systems Science in Metallurgical Process, The State Key Laboratory for Refractories and Metallurgy, Collaborative Innovation Center for Advanced Steels, International Research Institute for Steel Technology, Wuhan University of Science and Technology, Wuhan 430081, China
2 Key Laboratory of Artificial Micro- and Nano-structures of Ministry of Education and School of Physical and Technology, Wuhan University, Wuhan 430072, China
3 College of Advanced Interdisciplinary Studies, Nanhu Laser Laboratory, National University of Defense Technology, Changsha 410073, China
4 Department of Mechanical Engineering, National University of Singapore, Singapore 117575, Singapore
5 i-Lab & Key Laboratory of Nanodevices and Applications & Key Laboratory of Nanophotonic Materials and Devices, Suzhou Institute of Nano-Tech and NanoBionics, Chinese Academy of Sciences, Suzhou 215123, China
6 Institute of Optical Science and Technology, School of Physics and Astronomy, Shanghai Jiao Tong University, Shanghai 200240, China
[*]These authors contributed equally to this work.
Corresponding authors. E-mail: [†]sczhu@wust.edu.cn, [‡]wujian15203@163.com

Received September 22, 2023; accepted November 9, 2023

ABSTRACT

Currently, magnetic storage devices are encountering the problem of achieving lightweight and high integration in mobile computing devices during the information age. As a result, there is a growing urgency for two-dimensional half-metallic materials with a high Curie temperature (T_C). This study presents a theoretical investigation of the fundamental electromagnetic properties of the monolayer hexagonal lattice of Mn_2X_3 (X = S, Se, Te). Additionally, the potential application of Mn_2X_3 as magneto-resistive components is explored. All three of them fall into the category of ferromagnetic half-metals. In particular, the Monte Carlo simulations indicate that the T_C of Mn_2S_3 reaches 381 K, noticeably greater than room temperature. These findings present notable advantages for the application of Mn_2S_3 in spintronic devices. Hence, a prominent spin filtering effect is apparent when employing non-equilibrium Green's function simulations to examine the transport parameters. The resulting current magnitude is approximately 2×10^4 nA, while the peak gigantic magnetoresistance exhibits a substantial value of 8.36×10^{16} %. It is noteworthy that the device demonstrates a substantial spin Seebeck effect when the temperature differential between the electrodes is modified. In brief, Mn_2X_3 exhibits outstanding features as a high T_C half-metal, exhibiting exceptional capabilities in electrical and thermal drives spin transport. Therefore, it holds great potential for usage in spintronics applications.

Keywords half-metals, Mn_2X_3, high Curie temperature, electrical and thermal GMR

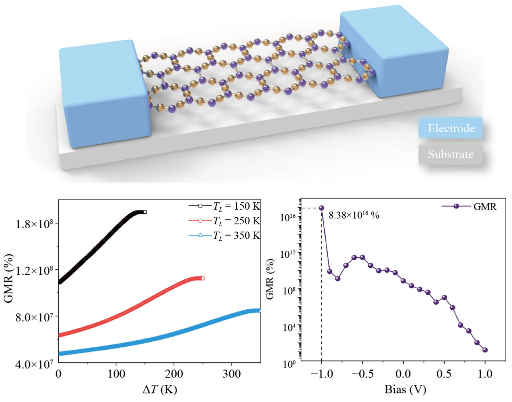

[#]Special Topic: Two-dimensional Electronic Materials and Devices (Eds.: Lin Wang & Xiaolong Chen).

Higher Education Press

https://doi.org/10.1007/s11467-023-1367-2

1 Introduction

Since the advent of von Neumann architecture computing devices, the field of information technology, particularly artificial intelligence, has generated remarkably creative data through the utilization of efficient cluster computing [1–3]. As a result of the escalating requirement for data storage and transfer, existing memory technologies such as Dynamic Random Access Memory, Static Random Access Memory, and NAND flash have proven inadequate in fulfilling the prevailing demand. As a result, the semiconductor industry has been pushed to investigate emerging semiconductor technologies that provide enhanced storage efficiency and decreased costs [4–7]. The magnetic storage device based on electron spin technology, is non-volatile, theoretically providing infinite read and write times, currently leads the industry in integration with logic chips, and performed better in our previous studies [8, 9]. At the same time, the write speed is fast, and the write time can be as low as nanoseconds [10]. Hence, there has been significant interest in spin and thermal spin memory devices as a viable answer to the existing challenge posed by reluctance equipment [11]. Spintronic focuses on the manipulation of electron spin and electron transport. It involves utilizing the spin state of electrons for the purposes of data storage, transmission, and retrieval. Moreover, spin thermoelectrics principally focus on the examination of heat and spin transport phenomena. In this paper, the exploitation of temperature gradients enables the movement of charge and spin [12]. In general, the major material carrier of the two technologies is half-metal material, which acts as a semiconductor or insulator in one spin channel, while the other channel can pass through the Fermi level. Consequently, the utilization of half-metal (HM) magnetoresistive devices enables the attainment of a 100% spin filtering effect (SFE), thereby demonstrating exceptional magnetoresistive propertiesin in our previous research [13–15]. The use of traditional materials in memory structures poses challenges for achieving high degrees of integration in modern mobile computing devices and Ultra-Large Scale Integrated Circuits (ULSICs). These traditional materials may not be suitable for meeting the requirements of lightweight devices. As a result, the development of ULSICs is hindered [16, 17]. The advent of low dimensional materials with atomic-scale thin film structures have brought a new dawn to magnetic storage devices [18]. In comparison to traditional materials, low-dimensional materials have favorable attributes such as regulated thickness and decreased power usage. In addition, it is noteworthy that low-dimensional materials possess a remarkable ability to alter interfaces [19–21]. The utilization of interface control in the fabrication of magnetoresistive devices using low-dimensional materials enables the attainment of enhanced spin polarization efficiency and improved magnetic stability [22]. In addition, 2D materials have many other special electronic structures and excellent properties, such as high carrier mobility and regulated band structure [23–25]. Therefore, it is obvious that 2D materials have significant promise for application in the field of spintronic devices.

Nevertheless, whereas 2D materials exhibit potential advancements in the field of magnetic storage devices, they also present novel challenges. Conventional materials possess a significantly greater volume in comparison to 2D materials due to their composition of many layers of atoms [26], the presence of dimensional constraints in 2D materials imposes limitations on the available spin degrees of freedom, hence restricting magnetic exchange interactions and spin-wave excitations. Consequently, in high-dimensional materials, spin-wave excitation can provide additional thermal excitation energy, helping to maintain a high Curie temperature (T_C) [27–30]. However, in low-dimensional materials, where spin-wave excitation is constrained by the scale, the energy of spin-wave excitation is relatively low, and as the temperature increases, the thermal fluctuation effect makes the direction of the spins more random, the ordering of the spins is weakened, and the magnetisation strength is reduced, making it difficult to maintain a higher T_C [31–33]. The lower T_C undoubtedly has a greatly impact on magnetic storage at room temperature. Therefore, low-dimensional materials with high T_C have always been the goal of researchers [34]. The Honeycomb Kagome (HK) lattice has gained significant attention in recent years due to its remarkable characteristics, such as high T_C, half-metallicity, and spin-gapless semiconductor (SGS) behavior [35–37]. For example, the HK-structured Nb_2O_3 with a high $T_C = 392$ K [38]. The Cr-based HK structure is a Dirac HM with a gap in theory, T_C values above 400 K, and large in-plane magnetic anisotropy energy, excellent SFE [39]. Simultaneously, the HK lattice exhibits considerable research promise through numerous predictions and experiments. In 2013, The study conducted by Addou *et al.* [40] provided evidence of the ability of Y_2O_3 to form fully formed monolayers on graphene substrates supported by platinum. Monolayers interact weakly with graphene, but are stable to high temperatures. This was also demonstrated by scanning tunneling microscopy and X-ray. In 2016, Song *et al.* [41] conducted a study examining the structural characteristics and properties of a monolayer of Al_2O_3. Their findings indicated the potential for experimental investigations in this structure. The researchers also made predictions regarding the significant band shift observed between the Al_2O_3 monolayer and graphene. Moreover, experimental fabrication of the ultrathin Cr_2O_3 by rapid thermal annealing that suggests the viability of synthesizing 2D Cr_2O_3 motivates us to explore the M_2X_3 [42]. However, there is still a lack of theoretical research on Mn_2X_3, especially on its spin transport [43, 44]. Therefore, it is meaningful to analyze Mn_2X_3 in theory for improving the 2D Mn-based material library.

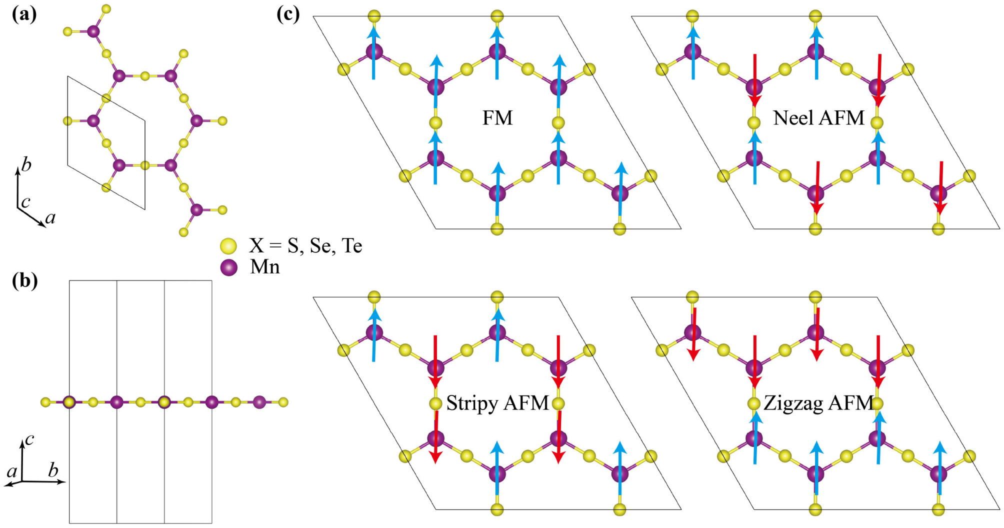

Fig. 1 Mn_2X_3 crystal structure and magnetic ground states. **(a)** Top, and **(b)** side views of Mn_2X_3 (X = S, Se, Te) monolayers, yellow indicates non-metallic elements, and purple is Mn. **(c)** FM configuration and three AFM configurations of Mn_2X_3 monolayers, red and blue indicate opposite spins.

In this paper, the electronic structure and magnetic properties of Mn_2X_3 (X = S, Se, Te) monolayer are systematically predicted by density functional theory (DFT). The T_C of Mn_2X_3 was further evaluated by Monte Carlo simulation. Moreover, a high T_C spin-reluctance device is designed based on Mn_2X_3, and the spin and thermal spin transport properties are simulated by non-equilibrium Green's function (NEGF). The evaluation of the SFE and giant magnetoresistive effect in Mn_2X_3 devices is conducted by the application of bias voltage and temperature variation. The findings of this study contribute to the expansion of the current database on 2D intrinsic half-metallic ferromagnets, offering a feasible experimental platform for the development of monolayer ferromagnetic materials and 2D spintronic devices.

2 Calculation method

The DFT for structure optimization and performance simulation is implemented in Quantum ATK packages and VASP packages. Use generalized gradient approximation (GGA-PBE) functional and Projector Augmented Wave (PAW) potential. When relaxation is performed, the set of 9 × 9 × 1 k points is used to sample the Brillouin zone. The convergence parameter of the total energy tolerance is set to 1×10^{-6} eV/atom, and the maximum force tolerance is set to 0.05 eV/Å for optimization. According to the relevant literature, the U value of 4 eV was set to the 3d orbit of transition metal Mn [45–48]. The vacuum layer along the z-axis is adjusted to 25 Å and fixed to avoid interaction between the slabs. The sampling of the set of the device is 1 × 5 × 100. Then, the spin resolved electron transport properties of these junctions are studied in the form of NEGF implemented. The electrically-driven spin transport performance can be quantitatively analyzed from the Landauer–Buttiker equation:

$$I(V_b) = \frac{2e^2}{h}\int_{-\infty}^{+\infty} T(E,V_b)\left[f_L(E-\mu_L) - f_R(E-\mu_R)\right]\mathrm{d}E. \tag{1}$$

Analogously, the spin resolved current driven by temperature difference ($\Delta T = T_L - T_R$) described using the following equation:

$$I = \frac{2e^2}{h}\int_{-\infty}^{+\infty} T(E)\left[f_L(E,T_L) - f_R(E,T_R)\right]\mathrm{d}E, \tag{2}$$

where T_L and T_R represent the temperatures of the left and right electrodes, respectively.

3 Results and discussion

Figures 1(a) and (b) are the cell geometry of the Mn_2X_3 monolayer, with lattice constants of 7.8 Å, 7.4 Å, and 9.0 Å for Mn_2S_3, Mn_2Se_3, and Mn_2Te_3 in Table S1 of the Electronic Supplementary Materials (ESM), respectively. Furthermore, we have successfully established the thermal stability of the monolayer Mn_2X_3 through the implementation of molecular dynamics simulations, as illustrated in Fig. S1 of the ESM. To evaluate stability of Mn_2X_3, an analysis of the phonon dispersion relations was performed, as depicted in Fig. S2 of the ESM. For the Mn_2X_3 structures, there are no imaginary frequencies in the Brillouin zone, proving the stability of all the systems investigated [49, 50]. To investigate the magnetic interactions, four possible magnetic ground

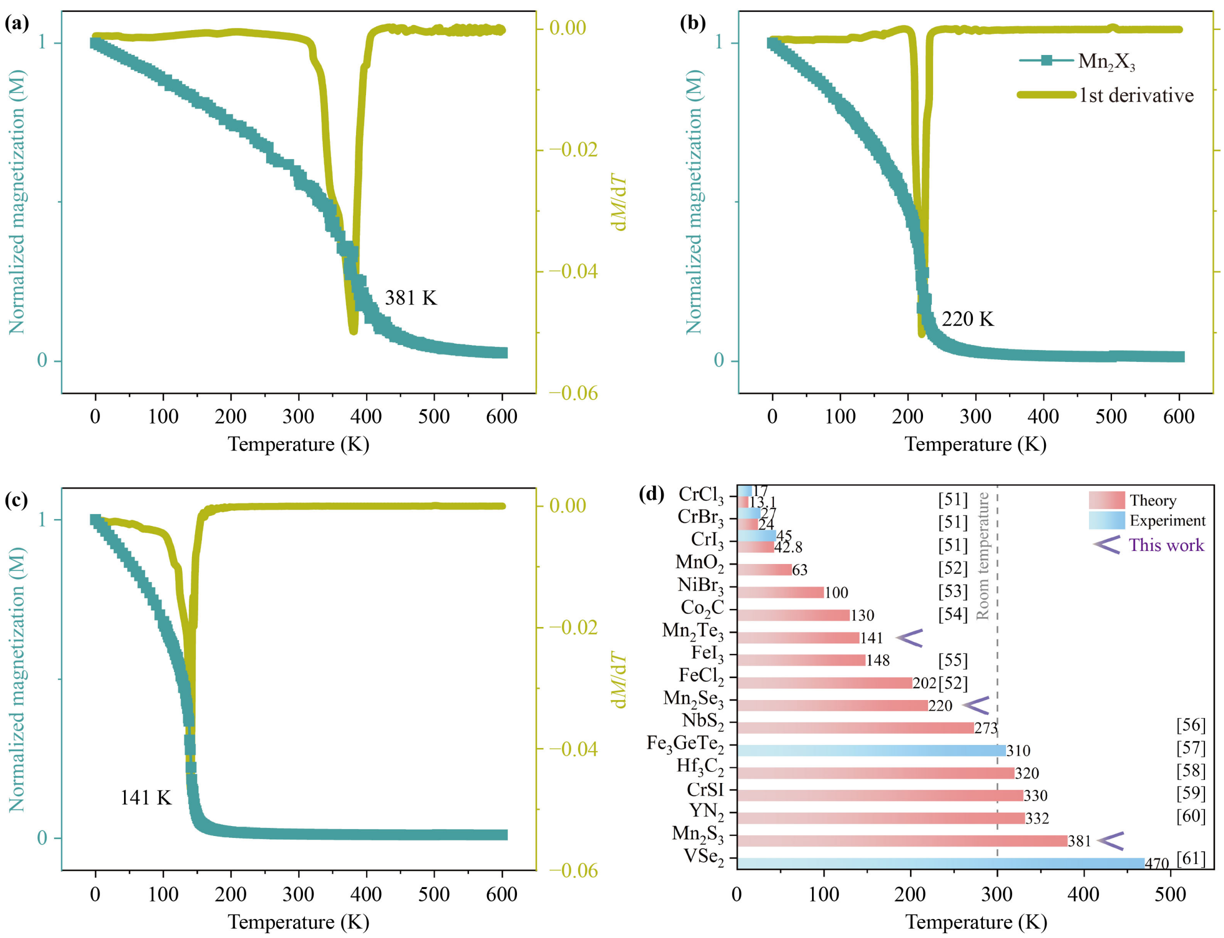

Fig. 2 Curie temperature of Mn_2X_3. Curie temperature (T_C) of Mn_2S_3, Mn_2Se_3, and Mn_2Te_3 in **(a)**, **(b)**, and **(c)**, respectively. **(d)** The Curie temperature of common 2D materials and Mn_2X_3.

states (MGSs) are considered in the 2 × 2 × 1 supercell: ferromagnetic (FM), stripy antiferromagnetic (AFM), Neel antiferromagnetic, and zigzag antiferromagnetic state. In Fig. 1(c), red and blue indicate opposite directions. The energy differences between the four MGSs have been computed and are summarized in Table S1 of the ESM, indicating that FM configuration is the most favorable MGS.

Moreover, the Monte Carlo approach is employed to simulate the alteration of the magnetic moment, as depicted in Fig. 2. In this representation, the magnetic moments are normalized, and the utilization of the first derivative enhances the clarity of the magnetic moment change. The simulation results show that the estimated T_C values of Mn_2S_3, Mn_2Se_3, and Mn_2Te_3 monolayers are 381 K [Fig. 2(a)], 220 K [Fig. 2(b)], and 141 K [Fig. 2(c)], respectively. Figure 2(d) presents a comparison between the Curie temperature of Mn_2X_3 and that of commonly 2D materials [51–61]. The interaction exchange between manganese (Mn) atoms and sulfur (S) atoms is relatively significant, and Mn_2S_3 exhibits a high Curie temperature. This notable high T_C of Mn_2S_3 bears important value in broadening the potential application scenarios of magnetoresistive devices that rely on ferromagnetic materials.

To gain insights into the electrical characteristics of the Mn_2X_3 monolayer, an investigation was conducted to study the potential utility of Mn_2X_3 in spintronics devices. This investigation involved the calculation of spin-resolved band structures and momentum-integrated spectral functions (usually called density of states, DOS), as depicted in Fig. 3. Figure 3(a) shows the Brillouin zone path. The fat band structures and orbital resolved DOS about Mn_2S_3 in Fig. 3(b), Mn_2Se_3 in Fig. 3(c), and Mn_2Te_3 in Fig. 3(f). The spin-up band of Mn_2S_3 in Fig. 3(b) intersects the Fermi level, whereas the spin-down channels are characterized by their insulating behavior. Consequently, the monolayers exhibit a half-metallic structure, with a spin polarization of 100% near the Fermi level. The presence of bands near the Fermi level in monolayers is mostly attributed to the spin-up orbitals of S elements. The spin-up orbitals are mostly influenced by the p_z orbitals of S elements, as determined through the examination of the density of states. Mn_2Se_3 and Mn_2Te_3, shown in Figs. 3(c) and (d), also exhibit similar properties to Mn_2S_3, and their nonmetallic

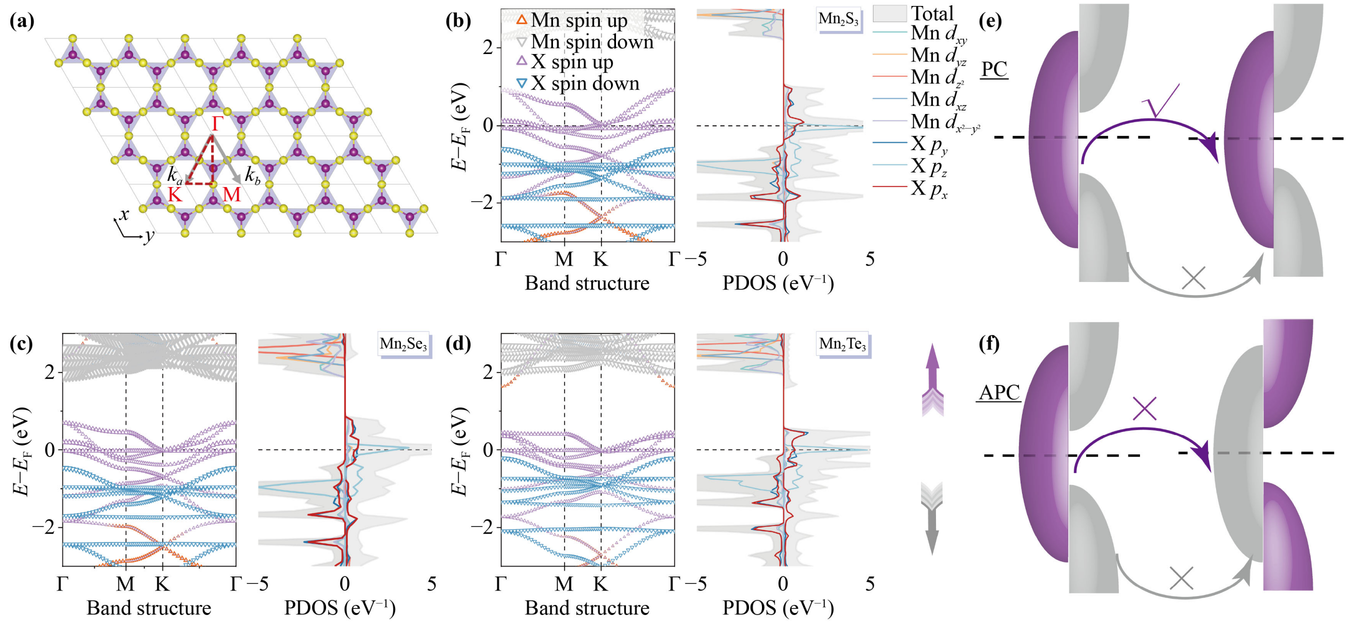

Fig. 3 Electromagnetic properties of Mn_2X_3 and half-metallic transport diagram. **(a)** The Brillouin zone path of Mn_2X_3. Band structure and DOS of Mn_2X_3 in **(b)**, **(c)**, and **(d)**, respectively. Electron transport models based on half-metallic materials with electrons in parallel **(e)** and anti-parallel configurations **(f)**, respectively.

elements are more likely to cross the Fermi level. Figure S3 of the ESM presents the results of band structure calculations conducted using the PBE and HSE06 methods, which suggest that the half-metallic properties of Mn_2X_3 can be well maintained, and the effect of spin–orbit coupling is considered in Fig. S4 of the ESM [50, 62].

In general, half-metallic materials and a variety of spin gapless semiconductors (SGSs) have excellent spin transport performance [63, 64]. Broadly speaking, the concept of SGS can be classified into two distinct groups, namely PSGSs and LSGSs [65, 66]. In particular, PSGSs or LSGSs can be classified into four distinct categories (Fig. S5 of the ESM) [67, 68]. Due to the half-metallic properties of Mn_2X_3, Figs. 3(e) and (f) show the common spin transport mechanisms of half-metallic that are specifically illustrated. When the electrodes are in a parallel magnetic configuration, the bands of the two electrodes are identical. Consequently, when a bias is applied, a polarization current is generated within the device. The generation of stable spin current in the device is hindered when the two electrodes are in antiparallel magnetic configuration. Therefore, the ideal spin reluctance can be obtained by adjusting the magnetic field of devices designed with half-metallic materials.

Therefore, based on the above analysis of T_C (up to 381 K) and half-metallic properties, Mn_2S_3 has a strong application potential in the field of spintronics devices. Therefore, we explore the possibility of Mn_2S_3 application in the realm of spintronics devices. A Mn_2S_3-based structure is placed in the center scattering region of the device, and the buffer region and the left and right electrode regions are each one supercell of Mn_2S_3 in Fig. 4(a). This study investigates two distinct magnetization configurations for the left and right electrodes, namely the parallel-configuration (PC) and the antiparallel-configuration (APC). In the context of PC, it is observed that both electrodes exhibit identical spin orientations, however in the APC, the electrodes demonstrate opposing spin orientations. The spin-dependent current–voltage (I–V) characteristics in both the parallel configuration and antiparallel configuration are illustrated in Fig. 4(b). In the PC, the spin-up current exhibits an initial increase as the bias is increased, reaching its maximum value at 0.4 V, after which it subsequently drops. In contrast, the current in the spin-down is effectively inhibited. In the case of APC, it can be observed that both spin currents experience a significant reduction in their magnitudes. Hence, the devices fabricated using monolayer Mn_2S_3 demonstrate the ideal SFE, the giant magnetoresistance (GMR) phenomenon, and the negative differential resistance effect. To more accurately characterize the exact value of the spin polarization (SP), we calculated the SFE under two magnetization states according to the formula $SP=\frac{I_{\rm up}-I_{\rm down}}{I_{\rm up}+I_{\rm down}}\times 100\%$, and it can be seen that the SP reaches almost 100% at all biases in the inset of Fig. 4(b). In addition, the value of the giant magnetoresistance effect was calculated according to the formula $GMR=\left|\frac{I_{\rm PC}-I_{\rm APC}}{I_{\rm APC}}\right|\times 100\%$, which can be seen in Fig. 4(c). It is worth mentioning that at zero bias, the calculation of SP and GMR depends on the transmission coefficient. The giant magnetoresistance effect can reach 8.38×10^{16} %

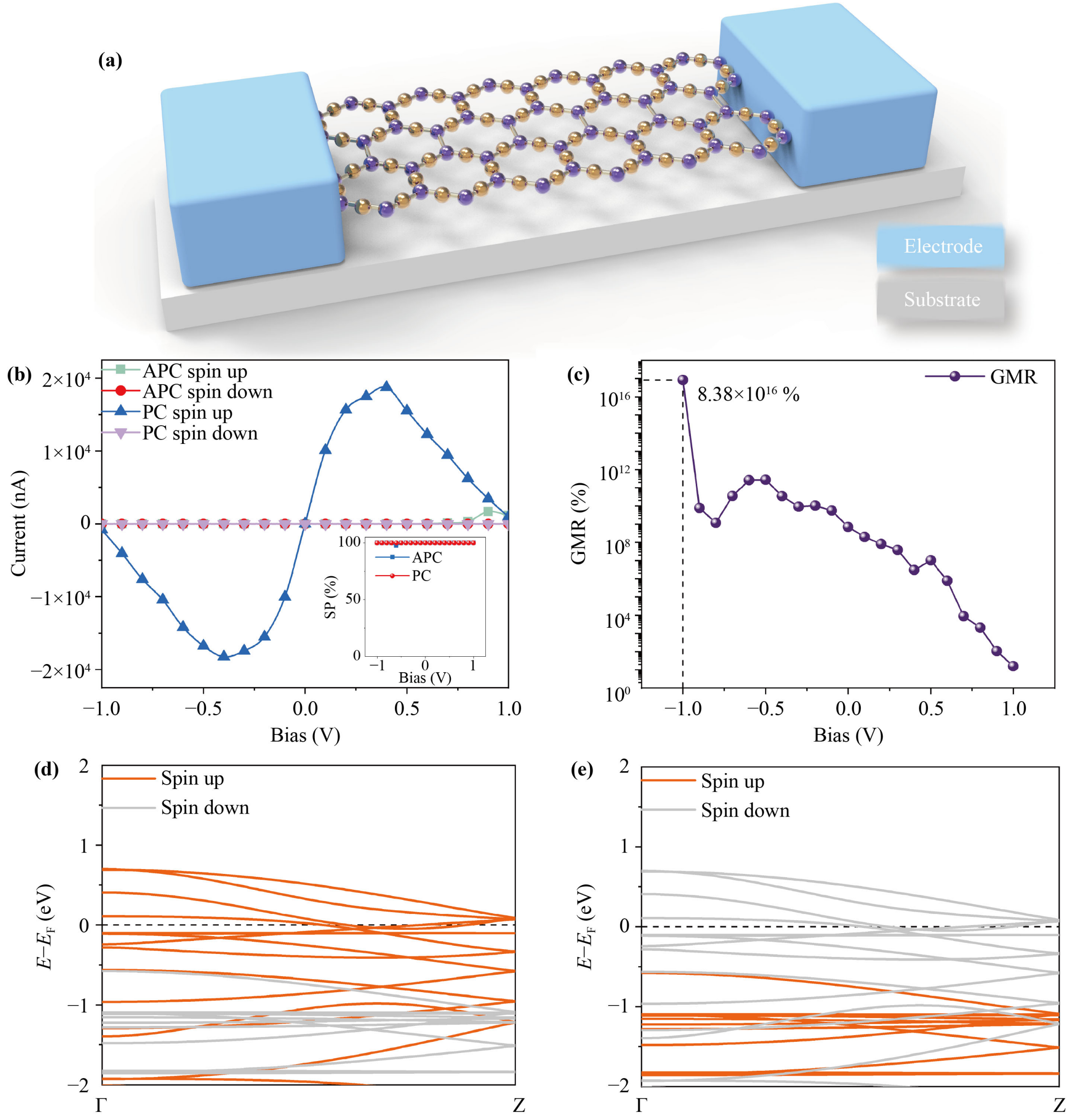

Fig. 4 Performance at two magnetization configurations (PC and APC) of devices based on Mn_2S_3. **(a)** A diagram of the device model. **(b)** The spin-resolved *I*–*V* curves. **(c)** Giant magnetoresistive. **(d, e)** The spin resolved band structures of electrodes at two magnetization configurations.

at –1.0 V bias where the current of APC is close to zero. Even rarer is the fact that under two-electrode voltage control, the voltage is within 0.6 V and the GMR can be maintained close to 10^5 %. It is noteworthy to emphasize that the current at the peak GMR (including the range from −1 V to −0.5 V) exhibits a minuscule and nearly imperceptible magnitude (APC current is on the order of 10^{-13} nA). Nevertheless, when the bias voltage is set to –0.4 V, a substantial rise in current is observed, while the magnetoresistance value remains consistently over 10^{10} %. In the context of a limited bias range, the remarkable GMR shows the potential application of Mn_2S_3 in electrically driven giant magnetoresistive devices.

The band structure of a device, namely in the direction of electrode transport in both PC and APC, frequently serves as a means to elucidate the underlying physical principles governing the relationship between current and bias voltage. Figures 4(d) and (e) are the electrode bands for different magnetic configurations, respectively. When a bias is applied to the electrode, the Fermi level of the left (right) electrode will shift downward (upward). Conversely, when a reverse bias is applied, the Fermi level will shift upward (downward). In the PC, the left and right electrodes have the same magnetization direction. As a result, they exhibit an identical band structure [Fig. 4(d)]. The spin bands consistently intersect the Fermi level, irrespective of whether the Fermi level shifts upwards or downwards. This implies that a spin-up transport channel always exists whenever a bias or

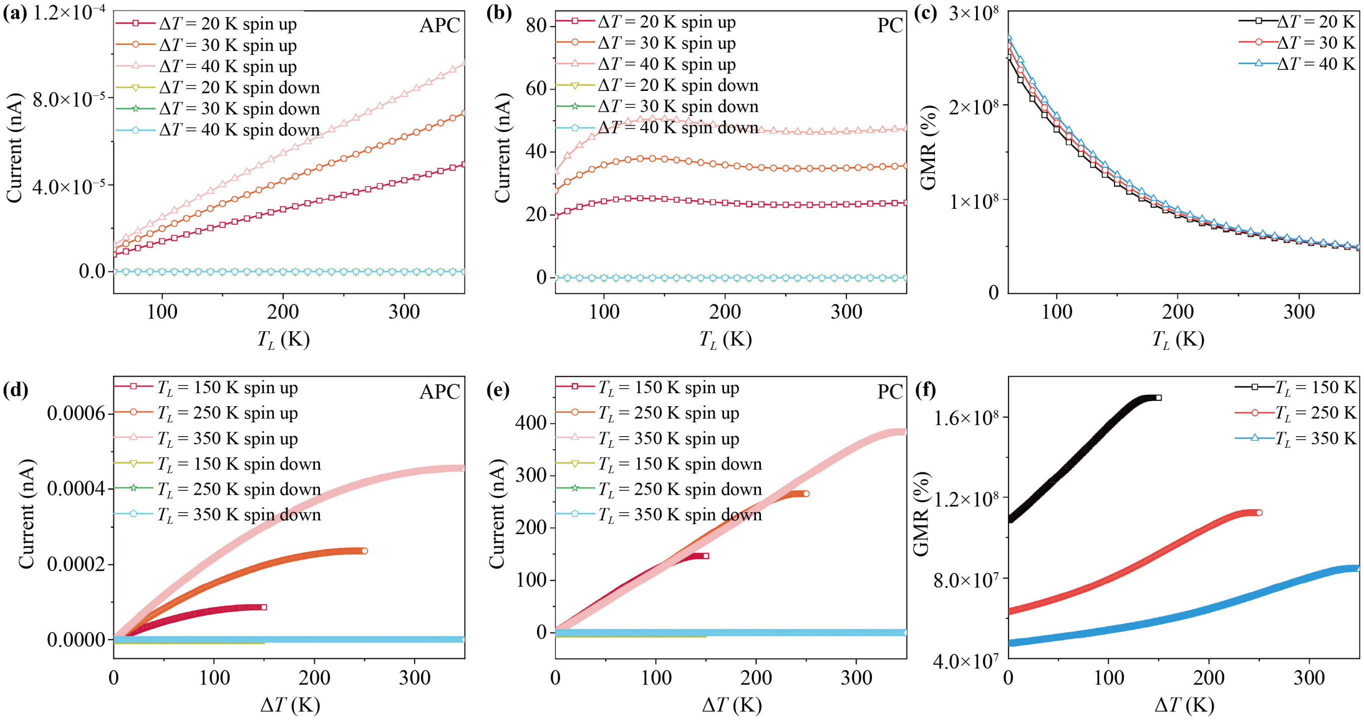

Fig. 5 Thermal spin performance of devices. The thermal spin resolved current with ΔT fixed for the device in the **(a)** APC and **(b)** PC. **(c)** Thermally induced GMR versus T_L. The thermal spin-resolved current when T_L fixed for the device in the **(d)** APC and **(e)** PC. **(f)** Thermally induced GMR versus ΔT.

reverse bias is applied. As the bias voltage increases, more bands come into contact with the Fermi level, thus increasing the number of available transport channels and the spin current. When the bias voltage exceeds approximately 0.4 V, there is a reduction in the number of bands that cross the Fermi level. As a result, the current decreases as the bias voltage increases, leading to the occurrence of negative differential resistance in the spin-up channel. The spin-down band remains significantly distant from the Fermi level, making it unable to contribute to a transport channel. This suppression of the spin-down current leads to excellent SFE. For the APC, the left electrode's band structure is shown in Fig. 4(d), while the right electrode's band structure is shown in Fig. 4(e), respectively. When a bias voltage is applied, only support spin-up transmission channels in the left electrode, while the right electrode can only support spin-down transmission channels. Due to the limited bias voltage, it is not possible for both the left and right electrodes to have transmission channels simultaneously. Consequently, the current at APC is suppressed, and the device produces a high giant magnetoresistance effect.

Moreover, owing to the high T_C of Mn_2S_3, it is of practical significance to study the temperature difference (ΔT) between the two electrodes in the intrinsic state of the device. In the simulation, since the simulation is based on the electron transmission coefficient, the temperature (difference) is the electron temperature (difference). We consider the spin currents as a function of left electrode temperature (T_L) for varying values of ΔT, and ΔT for different values of T_L. It is clear at APC from Fig. 5(a) that the current in spin-up channel increases with the enhancement of T_L when the ΔT fixed, and the current in spin-down channel is closed to zero over the whole range of T_L. The PC shown in Fig. 5(b), it is noteworthy that the spin-down current tends towards a negligible 0 nA, whilst the spin-up current exhibits a considerably larger increase as compared to the APC. Moreover, as the temperature T_L grows, the current exhibits a tendency to attain a peak level of consistent convergence, and the magnitude of this peak is directly correlated with the temperature disparity. The change of the thermionic giant magnetoresistance effect was determined while keeping ΔT constant. It was observed that the GMR decreases as T_L increases and the magnitude of the giant magnetoresistance effect is directly proportional to the magnitude of the temperature differential [Fig. 5(c)]. When T_L is fixed and ΔT is varied, the spin-up current increases with T_L, and the current in spin-down channel is almost 0 nA over the whole range of T_L [Fig. 5(d)]. In the depicted PC illustrated in Fig. 5(e), the thermal current exhibits a comparable trend to that observed in the APC setup. Notably, elevated temperatures frequently lead to a notable increase in current magnitude. Concurrently, in both APC and PC, there is a propensity for the current to converge with the escalation of temperature differential

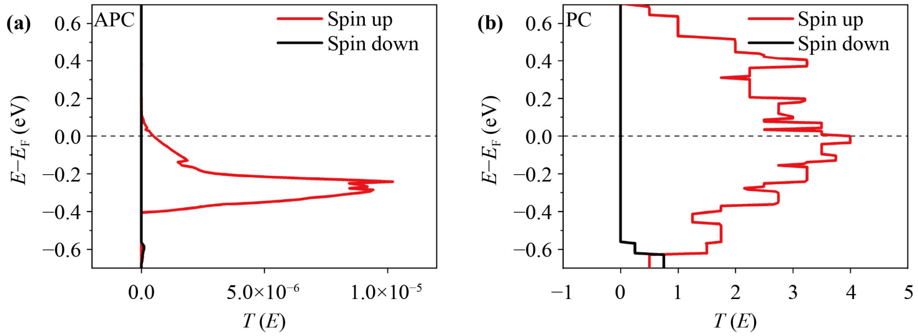

Fig. 6 Transport spectra of the device. Spin-dependent transport spectra of the devices in the **(a)** APC and **(b)** PC at zero bias.

between the electrodes. Figure 5(f) is the GMR value for the temperature of a fixed T_L, while the current changes with ΔT. It is evident that when the temperature difference rises, the GMR exhibits a progressive increase. In a similar vein, it can be shown that an increase in electrode temperature results in a decrease in the GMR when subjected to the same ΔT. However, it is worth noting that the GMR can still be sustained at a level above 10^7 %. Additionally, we calculated the thermal spin-filtering effect in these four cases (Fig. S6 of the ESM), and the SP can reach 100% at ΔT fixed as well as at T_L fixed.

In a thermal transport process, carriers such as electrons and holes tend to flow from higher temperature electrodes to lower temperature electrodes. When the energies of these carriers are below (or above) the Fermi level, holes (or electrons) act as the main migrating carriers, respectively. Figures 6(a) and (b) illustrate that the transport coefficient in spin-down channel remains consistently at zero and does not intersect with the Fermi level over a substantial energy range at APC. This suggests that spin-down carriers make negligible contributions to thermal transport. Therefore, the spin-down current is effectively zero. On the other hand, the spin-up transport coefficient crosses the Fermi level, indicating that both electrons and holes contribute to spin transport. The relative sizes of the regions below and above the Fermi level can be inferred from the energy and transport coefficients. It can be observed that the region below the Fermi level is greater than the region above the Fermi level. This observation suggests that the major mechanism for thermal transport in relation to spin is mostly influenced by the presence of holes, resulting in the generation of a positive spin current. As a result, the transfer of heat through the material becomes completely spin-polarized, resulting in a thermal spin-filtering phenomenon. Simultaneously, it is seen that the transport coefficient of PC surpasses that of APC, indicating the potential for the device to demonstrate significant thermal GMR. Hence, Mn_2S_3 monolayers exhibiting a high Curie temperature are regarded as promising contenders for spintronic and spin thermionic applications.

4 Conclusion

This study aims to examine the Mn_2X_3 monolayer, a 2D material, with a specific focus on the analysis of its electronic structure and spin transport performance. Through our analysis, all three are ferromagnetic half-metals. In particular, the T_C of Mn_2S_3 to reach 381 K is simulated by Monte Carlo, which is higher than room temperature and provides advantages for spintronic devices. Additionally, the spin devices constructed by Mn_2S_3 demonstrate considerable transport potentials. The giant magnetoresistance effect can reach 8.38×10^{16} % under −1 V when the I–V characteristics of the device are examined at −1 V. In addition, the Mn_2S_3 monolayer can show excellent thermally placed giant magnetoresistance effect and spin filtration effect under temperature difference, which makes it useful in spintronics and spintronic applications.

Declarations The authors declare that they have no competing interests and there are no conflicts.

Electronic supplementary materials The online version contains supplementary materials available at https://doi.org/10.1007/s11467-023-1367-2 and https://journal.hep.com.cn/fop/EN/10.1007/s11467-023-1367-2.

Acknowledgements This work was supported by the National Natural Science Foundation of China (Grant Nos. 11704291 and 12174296), the Hubei Province Key Laboratory of Systems Science in Metallurgical Process of Wuhan University of Science and Technology (Grant Nos. Y202101 and Y202208), the Scientific research project of Education Department of Hubei Province (Grant No. 2022024), the Postgraduate Scientific Research Innovation Project of Hunan Province (Grant No. QL20230006), and the High-Performance Computing Center of Wuhan University of Science and Technology. S. C. Z. also acknowledges the support from China Scholarship Council.

References

1. H. Bian, Y. Y. Goh, Y. Liu, H. Ling, L. Xie, and X. Liu,

Stimuli-responsive memristive materials for artificial synapses and neuromorphic computing, *Adv. Mater.* 33(46), 2006469 (2021)

2. D. Kim, B. Jeon, Y. Lee, D. Kim, Y. Cho, and S. Kim, Prospects and applications of volatile memristors, *Appl. Phys. Lett.* 121(1), 010501 (2022)
3. Z. Zhou, F. Yang, S. Wang, L. Wang, X. Wang, C. Wang, Y. Xie, and Q. Liu, Emerging of two-dimensional materials in novel memristor, *Front. Phys.* 17(2), 23204 (2022)
4. S. Hamdioui, H. Aziza, and G. C. Sirakoulis, Memristor based memories: Technology, design and test, in: 2014 9th IEEE International Conference on Design & Technology of Integrated Systems in Nanoscale Era (DTIS), 2014, pp 1–7
5. T. Endoh, 3D integration of memories including heterogeneous integration, in: 2021 International Symposium on VLSI Technology, Systems and Applications (VLSI-TSA), 2021, pp 1–2
6. S. Ikegawa, F. B. Mancoff, and S. Aggarwal, Commercialization of MRAM – Historical and future perspective, in: 2021 IEEE International Interconnect Technology Conference (IITC), 2021, pp 1–3
7. Q. Cao, W. Lü, X. R. Wang, X. Guan, L. Wang, S. Yan, T. Wu, and X. Wang, Nonvolatile multistates memories for high-density data storage, *ACS Appl. Mater. Interfaces* 12(38), 42449 (2020)
8. J. Puebla, J. Kim, K. Kondou, and Y. Otani, Spintronic devices for energy-efficient data storage and energy harvesting, *Commun. Mater.* 1(1), 24 (2020)
9. X. Zhang, P. Gong, F. Liu, K. Yao, J. Wu, and S. Zhu, High efficiency giant magnetoresistive device based on two-dimensional MXene (Mn_2NO_2), *Front. Phys.* 17(5), 53510 (2022)
10. X. Hu, D. Li, Y. Wang, J. Feng, Z. Ma, S. Wang, T. Min, X. Zeng, and Y. Xie, An 8Kb 40-nm 2T2MTJ STT-MRAM design with 2.6ns access time and time-adjustable writing process, in: 2021 IEEE 14th International Conference on ASIC (ASICON), 2021, pp 1–4
11. M. Hatami, G. E. W. Bauer, Q. Zhang, and P. J. Kelly, Thermal spin-transfer torque in magnetoelectronic devices, *Phys. Rev. Lett.* 99(6), 066603 (2007)
12. S. D. Sarma, Spintronics: A new class of device based on electron spin, rather than on charge, may yield the next generation of microelectronics, *Am. Sci.* 89(6), 516 (2001)
13. S. A. Wolf, D. D. Awschalom, R. A. Buhrman, J. M. Daughton, S. von Molnár, M. L. Roukes, A. Y. Chtchelkanova, and D. M. Treger, Spintronics: A spin-based electronics vision for the future, *Science* 294(5546), 1488 (2001)
14. C. Zheng, K. Jiang, K. Yao, S. Zhu, and K. Wu, The electromagnetic performance of transition metal-substituted monolayer black arsenic-phosphorus, *Phys. Chem. Chem. Phys.* 23(43), 24570 (2021)
15. S. C. Zhu, S. J. Peng, K. M. Wu, C. T. Yip, K. L. Yao, and C. H. Lam, Negative differential resistance, perfect spin-filtering effect and tunnel magnetoresistance in vanadium-doped zigzag blue phosphorus nanoribbons, *Phys. Chem. Chem. Phys.* 20(32), 21105 (2018)
16. Z. Cao, B. Sun, G. Zhou, S. Mao, S. Zhu, J. Zhang, C. Ke, Y. Zhao, and J. Shao, Memristor-based neural networks: A bridge from device to artificial intelligence, *Nanoscale Horiz.* 8(6), 716 (2023)
17. S. S. Iyer and B. Vaisband, Heterogeneous integration at scale, in: Advances in Semiconductor Technologies, Wiley, 2022, pp 1–24
18. B. Huang, G. Clark, E. Navarro-Moratalla, D. R. Klein, R. Cheng, K. L. Seyler, D. Zhong, E. Schmidgall, M. A. McGuire, D. H. Cobden, W. Yao, D. Xiao, P. Jarillo-Herrero, and X. Xu, Layer-dependent ferromagnetism in a van der Waals crystal down to the monolayer limit, *Nature* 546(7657), 270 (2017)
19. Y. Lv, W. Qin, C. Wang, L. Liao, and X. Liu, Recent advances in low-dimensional heterojunction-based tunnel field effect transistors, *Adv. Electron. Mater.* 5(1), 1800569 (2019)
20. S. Z. Butler, S. M. Hollen, L. Cao, Y. Cui, J. A. Gupta, H. R. Gutiérrez, T. F. Heinz, S. S. Hong, J. Huang, A. F. Ismach, E. Johnston-Halperin, M. Kuno, V. V. Plashnitsa, R. D. Robinson, R. S. Ruoff, S. Salahuddin, J. Shan, L. Shi, M. G. Spencer, M. Terrones, W. Windl, and J. E. Goldberger, Progress, challenges, and opportunities in two-dimensional materials beyond graphene, *ACS Nano* 7(4), 2898 (2013)
21. R. Guo, Y. Guo, Y. Zhang, X. Gong, T. Zhang, X. Yu, S. Yuan, and J. Wang, Electron doping induced stable ferromagnetism in two-dimensional GdI_3 monolayer, *Front. Phys.* 18(4), 43304 (2023)
22. J. F. Dayen, S. J. Ray, O. Karis, I. J. Vera-Marun, and M. V. Kamalakar, Two-dimensional van der Waals spinterfaces and magnetic-interfaces, *Appl. Phys. Rev.* 7(1), 011303 (2020)
23. C. Xin, J. Zheng, Y. Su, S. Li, B. Zhang, Y. Feng, and F. Pan, Few-layer tin sulfide: A new black-phosphorus-analogue 2D material with a sizeable band gap, odd–even quantum confinement effect, and high carrier mobility, *J. Phys. Chem. C* 120(39), 22663 (2016)
24. J. Cheng, C. Wang, X. Zou, and L. Liao, Recent advances in optoelectronic devices based on 2D materials and their heterostructures, *Adv. Opt. Mater.* 7(1), 1800441 (2019)
25. W. J. Yin, X. L. Zeng, B. Wen, Q. X. Ge, Y. Xu, G. Teobaldi, and L. M. Liu, The unique carrier mobility of Janus MoSSe/GaN heterostructures, *Front. Phys.* 16(3), 33501 (2021)
26. B. Mendoza-Sánchez and Y. Gogotsi, Synthesis of two-dimensional materials for capacitive energy storage, *Adv. Mater.* 28(29), 6104 (2016)
27. M. Fidrysiak and J. Spałek, Universal collective modes from strong electronic correlations: Modified $1/N_f$ theory with application to high-T_c cuprates, *Phys. Rev. B* 103(16), 165111 (2021)
28. P. Laurell and S. Okamoto, Dynamical and thermal magnetic properties of the Kitaev spin liquid candidate α-$RuCl_3$, *npj Quantum Mater.* 5, 2 (2020)
29. L. Zhang, C. Zhang, S. F. Zhang, W. Ji, P. Li, and P. Wang, Two-dimensional honeycomb-kagome Ta_2S_3: A promising single-spin Dirac fermion and quantum anomalous hall insulator with half-metallic edge states, *Nanoscale* 11(12), 5666 (2019)
30. Z. X. Shen, X. Bo, K. Cao, X. Wan, and L. He,

Magnetic ground state and electron-doping tuning of Curie temperature in Fe_3GeTe_2: First-principles studies, *Phys. Rev. B* 103(8), 085102 (2021)

31. S. K. Pati, S. Ramasesha, and D. Sen, Low-lying excited states and low-temperature properties of an alternating spin-1–spin-1/2 chain: A density-matrix renormalization-group study, *Phys. Rev. B* 55(14), 8894 (1997)
32. H. Wang, J. Qi, and X. Qian, Electrically tunable high Curie temperature two-dimensional ferromagnetism in van der Waals layered crystals, *Appl. Phys. Lett.* 117(8), 083102 (2020)
33. M. C. Wang, C. C. Huang, C. H. Cheung, C. Y. Chen, S. G. Tan, T. W. Huang, Y. Zhao, Y. Zhao, G. Wu, Y. P. Feng, H. C. Wu, and C. R. Chang, Prospects and opportunities of 2D van der Waals magnetic systems, *Ann. Phys.* 532(5), 1900452 (2020)
34. D. L. Cortie, G. L. Causer, K. C. Rule, H. Fritzsche, W. Kreuzpaintner, and F. Klose, Two-dimensional magnets: Forgotten history and recent progress towards spintronic applications, *Adv. Funct. Mater.* 30(18), 1901414 (2020)
35. J. Xing, X. Jiang, Z. Liu, Y. Qi, and J. Zhao, Robust Dirac spin gapless semiconductors in a two-dimensional oxalate based organic honeycomb-Kagome lattice, *Nanoscale* 14(5), 2023 (2022)
36. H. P. Wang, W. Luo, and H. J. Xiang, Prediction of high-temperature quantum anomalous Hall effect in two-dimensional transition-metal oxides, *Phys. Rev. B* 95(12), 125430 (2017)
37. X. K. Liu, X. Y. Li, M. J. Ren, P. J. Wang, and C. W. Zhang, High-temperature nodal ring semimetal in two-dimensional honeycomb-Kagome Mn_2N_3 lattice, *Chin. Phys. B* 31(12), 127203 (2022)
38. S. Zhang, C. Zhang, S. Zhang, W. Ji, P. Li, P. Wang, S. Li, and S. Yan, Intrinsic Dirac half-metal and quantum anomalous Hall phase in a hexagonal metal-oxide lattice, *Phys. Rev. B* 96(20), 205433 (2017)
39. J. Y. Chen, X. X. Li, W. Z. Zhou, J. L. Yang, F. P. Ouyang, and X. Xiong, Large-spin-gap nodal-line half-metal and high-temperature ferromagnetic semiconductor in Cr_2X_3 ($X = O$, S, Se) monolayers, *Adv. Electron. Mater.* 6(1), 1900490 (2020)
40. R. Addou, A. Dahal, and M. Batzill, Growth of a two-dimensional dielectric monolayer on quasi-freestanding graphene, *Nat. Nanotechnol.* 8(1), 41 (2013)
41. T. T. Song, M. Yang, J. W. Chai, M. Callsen, J. Zhou, T. Yang, Z. Zhang, J. S. Pan, D. Z. Chi, Y. P. Feng, and S. J. Wang, The stability of aluminium oxide monolayer and its interface with two-dimensional materials, *Sci. Rep.* 6(1), 29221 (2016)
42. C. Zhao, H. Zhang, W. Si, and H. Wu, Mass production of two-dimensional oxides by rapid heating of hydrous chlorides, *Nat. Commun.* 7(1), 12543 (2016)
43. Y. Feng, N. Liu, and G. Gao, Spin transport properties in Dirac spin gapless semiconductors Cr_2X_3 with high Curie temperature and large magnetic anisotropic energy, *Appl. Phys. Lett.* 118(11), 112407 (2021)
44. I. G. Dance and K. J. Fisher, Density functional calculations of electronic structure, geometric structure and stability for molecular manganese sulfide clusters, *J. Chem. Soc. Dalton Trans.* (15), 2563 (1997)
45. X. G. Li, J. N. Fry, and H. P. Cheng, Single-molecule magnet Mn_{12} on graphene, *Phys. Rev. B* 90(12), 125447 (2014)
46. A. Mabrouki, T. Mnasri, A. Bougoffa, A. Benali, E. Dhahri, and M. A. Valente, Experimental study and DFT calculation of the oxygen deficiency effects on structural, magnetic and optical properties of $La_{0.8\square0.2}MnO_{3-\delta}$ ($\delta = 0$, 0.1 and 0.2) compounds, *J. Alloys Compd.* 860, 157922 (2021)
47. R. Kaur, T. Maitra, and T. Nautiyal, Study of structural and electronic properties of Mn_3O_4, *AIP Conf. Proc.* 1591, 1137 (2014)
48. U. del Pennino, V. De Renzi, R. Biagi, V. Corradini, L. Zobbi, A. Cornia, D. Gatteschi, F. Bondino, E. Magnano, M. Zangrando, M. Zacchigna, A. Lichtenstein, and D. W. Boukhvalov, Valence band resonant photoemission of Mn_{12} single molecules grafted on Au(111) surface, *Surf. Sci.* 600(18), 4185 (2006)
49. G. Ding, C. Xie, J. Bai, Z. Cheng, X. Wang, and W. Wu, Recipe for single-pair-Weyl-points phonons carrying the same chiral charges, *Phys. Rev. B* 108(2), L020302 (2023)
50. G. Ding, C. Xie, J. Gong, J. Wang, J. Bai, W. Wang, D. Li, X. P. Li, and X. Wang, Exotic topological phonon modes in semiconductors: Symmetry analysis and first-principles calculations for representative examples, *Phys. Rev. B* 108(7), 075201 (2023)
51. X. Lu, R. Fei, and L. Yang, Curie temperature of emerging two-dimensional magnetic structures, *Phys. Rev. B* 100(20), 205409 (2019)
52. D. Torelli, K. S. Thygesen, and T. Olsen, High throughput computational screening for 2D ferromagnetic materials: The critical role of anisotropy and local correlations, *2D Mater.* 6, 045018 (2019)
53. J. Sun, X. Zhong, W. Cui, J. Shi, J. Hao, M. Xu, and Y. Li, The intrinsic magnetism, quantum anomalous Hall effect and Curie temperature in 2D transition metal trihalides, *Phys. Chem. Chem. Phys.* 22(4), 2429 (2020)
54. Y. Hu, X. Y. Liu, Z. H. Shen, Z. F. Luo, Z. G. Chen, and X. L. Fan, High Curie temperature and carrier mobility of novel Fe, Co and Ni carbide MXenes, *Nanoscale* 12(21), 11627 (2020)
55. Z. Guan and S. Ni, Strain-controllable high Curie temperature and magnetic crystal anisotropy in a 2D ferromagnetic semiconductive FeI_3 monolayer, *ACS Appl. Electron. Mater.* 3(7), 3147 (2021)
56. Y. Sun, Z. Zhuo, and X. Wu, Bipolar magnetism in a two-dimensional NbS_2 semiconductor with high Curie temperature, *J. Mater. Chem. C* 6(42), 11401 (2018)
57. Y. Deng, Y. Yu, Y. Song, J. Zhang, N. Z. Wang, Z. Sun, Y. Yi, Y. Z. Wu, S. Wu, J. Zhu, J. Wang, X. H. Chen, and Y. Zhang, Gate-tunable room-temperature ferromagnetism in two-dimensional Fe_3GeTe_2, *Nature* 563(7729), 94 (2018)
58. F. Zhou, Y. Liu, M. Kuang, P. Wang, J. Wang, T. Yang, X. Wang, Z. Cheng, and G. Zhang, Time-reversal-breaking Weyl nodal lines in two-dimensional A_3C_2 ($A =$ Ti, Zr, and Hf) intrinsically ferromagnetic materials with high Curie temperature, *Nanoscale* 13(17), 8235 (2021)
59. Z. Jiang, P. Wang, J. Xing, X. Jiang, and J. Zhao,

Screening and design of novel 2D ferromagnetic materials with high Curie temperature above room temperature, *ACS Appl. Mater. Interfaces* 10(45), 39032 (2018)

60. Z. Liu, J. Liu, and J. Zhao, YN_2 monolayer: Novel p-state Dirac half metal for high-speed spintronics, *Nano Res.* 10(6), 1972 (2017)
61. W. Yu, J. Li, T. S. Herng, Z. Wang, X. Zhao, X. Chi, W. Fu, I. Abdelwahab, J. Zhou, J. Dan, Z. Chen, Z. Chen, Z. Li, J. Lu, S. J. Pennycook, Y. P. Feng, J. Ding, and K. P. Loh, Chemically exfoliated VSe_2 monolayers with room-temperature ferromagnetism, *Adv. Mater.* 31(40), 1903779 (2019)
62. X. Zhang, X. Wang, T. He, L. Wang, W. Yu, Y. Liu, G. Liu, and Z. Cheng, Magnetic topological materials in two-dimensional: Theory, material realization and application prospects, *Sci. Bull. (Beijing)* 68(21), 2639 (2023)
63. X. L. Wang, Proposal for a new class of materials: Spin gapless semiconductors, *Phys. Rev. Lett.* 100(15), 156404 (2008)
64. G. Shan, Z. Ding, and Y. Gogotsi, Two-dimensional MXenes and their applications, *Front. Phys.* 18(1), 13604 (2023)
65. C. Fang, H. Weng, X. Dai, and Z. Fang, Topological nodal line semimetals, *Chin. Phys. B* 25(11), 117106 (2016)
66. Y. Li, Z. Zhou, P. Shen, and Z. Chen, Spin gapless semiconductor–metal–half-metal properties in nitrogen-doped zigzag graphene nanoribbons, *ACS Nano* 3(7), 1952 (2009)
67. Q. Gao, I. Opahle, and H. Zhang, High-throughput screening for spin-gapless semiconductors in quaternary Heusler compounds, *Phys. Rev. Mater.* 3(2), 024410 (2019)
68. S. D. Guo, Y. L. Tao, G. Wang, S. Chen, D. Huang, and Y. S. Ang, Proposal for valleytronic materials: Ferrovalley metal and valley gapless semiconductor, *Front. Phys.* 19(2), 23302 (2024)